CrystEngComm

Accepted Manuscript

ROYAL SOCIETY OF CHEMISTRY

www.rsc.org/crystengcomm

Controllable synthesis of "L"-shaped V_2O_5 and the improved adsorption capacity by fluorine

Yang Yang, Fei Teng*, Yandong Kan, Liming Yang, Wenhao Gu, Juan Xu, Yunxuan Zhao, Xi Du, Ming Ren

Jiangsu Engineering and Technology Research Center of Environmental Cleaning Materials (ECM), Jiangsu Key Laboratory of Atmospheric Environment Monitoring and Pollution Control (AEMPC), Jiangsu Joint Laboratory of Atmospheric Pollution Control (APC), Collaborative Innovation Center of Atmospheric Environment and Equipment Technology (AEET), School of Environmental Science and Engineering, Nanjing University of Information Science & Technology, 219 Ningliu Road, Nanjing

Abstract

In this work, V_2O_5 with an interesting "L"-shape is successfully prepared by a simple hydrothermal method without using any surfactant or template. The formation mechanism of "L"-shaped V_2O_5 has been proposed. We have also investigated the effect of fluoride on the morphology, crystal structure and adsorption ability of the samples. The samples are characterized by scanning electron microscopy (SEM), high-resolution transmission electron microscopy (HRTEM) with select area electron diffraction (SAED), X-ray diffraction (XRD), Fourier transform infrared spectrum (FT-IR), UV-vis diffuse reflectance spectra (UV-DRS), Photoluminescence (PL) spectra and N_2 sorption isotherms. It is found that the addition of fluoride can refrain the formation of "L"-shaped V_2O_5, resulting in the high-energy {010} facets exposed

* Corresponding author. Tel./Fax.: +86-25-9882-1090;Email address: tfwd@163.com

and the increased oxygen vacancy. The density functional theory (DFT) calculations and PL spectra further confirm the results above. As a result, F-doped V_2O_5 shows a significantly improved adsorption capacity for methylene blue (MB) than undoped one. The adsorption kinetics well follows a pseudo-second-order model, with the higher correlation coefficients (R) than 0.99.

Keywords: "L"-shaped V_2O_5; Fluorination; Adsorption; Density Functional Theory (DFT)

1. Introduction

Dyes and pigments are widely used in printing, pharmacy, textile, leather, food and cosmetics etc.[1,2] Dyes pollution has caused great attention due to its potential mutagenic and carcinogenic properties to environment and human health.[1] Therefore, it is necessary to use an effective way to remove dyes from wastewater before discharging. To date, various technologies including biotechnology, physical and chemical methods have been used to reduce the pollution and hazard of dyes.[2,3] Among these methods, adsorption is considered as one of the most economical and effective technologies to separate dyes from wastewater.[4,5] Up to now, many absorbents including biochar,[6,7] activated carbon,[8-10] graphene[11-13] and other metallic oxide or metal-organic frameworks[14,15] have been investigated to remove pollutants. However, the high cost or low adsorption capacities of absorbents is still a big challenge.[16] Hence, it is desirable to develop a high adsorption capacity, low cost, good chemical stability and easy recycled absorbent.

Herein, we have developed new V_2O_5 hierarchical nanostructures as an absorbent. V_2O_5 hierarchical nanostructures have attracted great attention due to its new nanostructure, physical and chemical properties.[14,17] It is widely accepted that small nanoparticles have a high adsorption capacity due to its large surface to volume ratio.[18] However, nanoparticles easily suffer from aggregation and are difficult to be separated from solution, which may cause secondary pollution.[13,14] Thus, the fabrication of hierarchically nanostructured adsorbents is desirable to avoid these

problems.[14]

Up to now, V_2O_5 with various morphologies including nanowires,[19,20] nanosheets,[21] naotubes,[22] nanorods,[23,24] nanobelts[25] and nanoflowers have been reported.[26-28]. Herein, we have developed a simple hydrothermal method to synthesize the new "L"-shaped V_2O_5 nanostructures, which have not been reported yet. It is amazing that the "L"-shaped V_2O_5 nanostructures exhibit a higher adsorption capacity for MB due to its larger surface area (17.7 m^2 g^{-1}) than that (5.8 m^2 g^{-1}) of V_2O_5 particle.

In addition, great attention has been paid to improve adsorption performances of common adsorbents by surface modification[13,29,30] or loading functional nanoparticles.[31-33] The graphene-V_2O_5 nanocomposite synthesized by Ramasamy et al.[30] showed an significantly enhanced photocatalytic performance for the degradation of methylene blue dye under sunlight. Wu et al.[29] used cetyltrimethylammonium bromide (CTAB) to modify graphene (GN), and the results showed that CTAB-GN shows a high adsorption capacity for Cr (VI) in aqueous solutions. The V_2O_5 also exhibited an high catalytic performance for selective catalytic reduction of NO_x.[34,35] Besides, V_2O_5 also has a wide application in ion battery field[36,37,38] because of its high theoretical capacity (440 mA h g^{-1})[39] and lower cost than CoO_x.[40] Additionally, the metal-doped V_2O_5, e.g., cooper, manganese, niobium, titanium silver and iron etc., also showed an improved performance.[31-33,41] However, little work has been conducted for anion-doped V_2O_5.

Herein, we employed F to dope V_2O_5 so as to improve its adsorption

performances. The results showed that doping of F not only increased the oxygen defect but also exposed the high-energy {010} facets, compared with the un-doped V_2O_5. Besides, the density functional theory (DFT) method has also been used to calculate the electronic structure, density of states and surface free energy of V_2O_5. The calculated results showed that the surface energy of (010) plane is obviously higher than that of (001) planes.

2. Experimental

2.1 Sample preparation

All reagents were of analytical grade, purchased from Beijing Chemical Reagents Industrial Company of China, and were used without further purification.

"L"-shaped V_2O_5. Typically, 2.4 mmol NH_4VO_3 was added into 20 mL of HNO_3 (65 *wt*%) solution at room temperature. After being stirred for 20 min, the solution was transferred into a 40-mL Teflon-lined stainless steel autoclave, followed by the hydrothermal treatment at 180 °C for 24 h. After the autoclave was cooled to room temperature naturally, the yellow precipitate was separated, washed, and dried at 60 °C for 4 h. The as-prepared sample was denoted as F0.

V_2O_5 nanowires. Firstly, 2.4 mmol NH_4VO_3 was dissolved in 20 mL of HNO_3 (65 *wt*%) solution at room temperature with stirring. After being stirred for 10 min, 2.4 mmol of NaF (V/F molar ratio) was added into the above solution. After another 20 min stirring, the mixture was transferred into a 40-mL Teflon-lined stainless steel autoclave, followed by the hydrothermal treatment at 180 °C for 24 h. After reaction, the yellow precipitate was separated, washed, and dried at 60 °C for 4 h. Herein, the molar ratio of V/F was varied from 1/1 to 1/2 and 1/4 to investigated the effect of NaF

amount added on the samples. The samples prepared at V/F=1/1, 1/2 and 1/4 were denoted as F1, F2 and F3, respectively. Furthermore, NaF was used to substituted by NH_4F and NaCl to investigate the effects of cation and anion on the samples, respectively; while keeping the other condition same.

2.2 Characterization

The crystal structures of the samples were determined by X-ray powder polycrystalline diffractometer (Rigaku D/max-2550VB), using graphite monochromatized Cu K_α radiation (λ= 0.154 nm), operating at 40 kV and 50mA. The XRD patterns were obtained in the range of 20-80° (2θ) at a scanning rate of 7 $^o min^{-1}$. The samples were characterized on a scanning electron microscope (SEM, Hitachi SU-1510) with an acceleration voltage of 15 keV. The samples were coated with 5-nm-thick gold layer before observations. The fine surface structures of the samples were determined by high-resolution transmission electron microscopy (HRTEM, JEOL JEM-2100F) equipped with an electron diffraction (ED) attachment with an acceleration voltage of 200 kV. X-ray photoelectron spectroscopy (XPS) measurements were done on a VG ESCALAB MKII XPS system with Mg K_α source and a charge neutralizer. All the binding energies were referenced to the C1s peak at 284.8 eV of the surface adventitious carbon. UV-vis diffused reflectance spectra of the samples were obtained using a UV-vis spectrophotometer (UV-2550, Shimadzu, Japan). $BaSO_4$ was used as a reflectance standard in a UV-vis diffuse reflectance experiment. Photoluminescence (PL) spectra were measured on a fluorescence spectrophotometer (Japan, Shimadzu RF-5301PC) with the 260 nm excitation line of a Xe lamp as the excitation source. Nitrogen sorption isotherms were performed at 77 K and < 10^{-4} bar on a Micromeritics ASAP2010 gas adsorption analyzer. Surface area

and the pore size distribution were calculated by the Brunauer-Emmett-Teller (BET) and Barret-Joyner-Halender (BJH) methods, respectively.

2.3 Adsorption performance

The adsorption performances of the samples were evaluated by removing methylene blue (MB) from aqueous solution. Typically, 0.025 g of powders was added into 20 mL of MB solution (10, 20, 50 and 100 mg L^{-1}). The suspension was stirred for 590 min to reach an adsorption–desorption equilibrium of dye molecules on the solid surface. During adsorption process, 3 mL of suspension was collected at a given time interval and centrifuged to remove the particles. The concentration of dye remaining in the solution was determined by UV-Vis spectrophotometry at 664 nm. All the adsorption tests were kept at 25±1 °C without adjusting pH of dye solution.

2.4 Theory calculation

The electronic structures of V_2O_5 was calculated by Density Functional Theory (DFT) with the generalized-gradient approximation (GGA) and the exchange–correlation functional of Perdew–Burke–Ernzerh of (PBE) using Materials Studios software and the CASTEP energy cutoff of 380 eV is adopted. The super cell of V_2O_5 was constructed by 40 oxygen and 16 vanadium atoms.

3. Results and discussion

3.1 Effects of reaction temperature and time

The temperature- and time-dependent experiments have been performed to investigate the effects of reaction temperature and time on the samples. First, the

hydrothermal temperature was varied from 120 to 140, 160 and 180 °C, while the other conditions were kept constant. Fig. 1 shows the SEM images and XRD patterns of the as-obtained samples. At lower temperatures (120, 140 and 160 °C), the as-prepared samples display irregular morphology (Fig. 1a-d). At 180 °C, the "L"-shaped V_2O_5 sample has formed, which consists of nanowires. As far as we know, this novel V_2O_5 "L"-shaped nanostructure has not been reported previously. Fig. 1e shows that the diffraction peaks of the as-obtained samples are very weak at 120 and 140 °C. At 160 and 180 °C for 24 h, the diffraction peaks of the sample become stronger. This results show that the reaction temperature has a significant influence on the crystallinity and morphology of the sample, and that 180 °C favors to form "L"-shaped V_2O_5.

Furthermore, hydrothermal time was varied from 3, 6, 12, 24 and 48 h to investigate the effect of reaction time while the other conditions were kept constant. Fig. 2a shows that all the diffraction peaks are well in accord with the V_2O_5 standard card (JCPDS no. 41-1426), revealing that phase-pure V_2O_5 can form at 3h. With increasing reaction time, the peak intensities of the samples increase gradually. Fig. 2(b-f) shows SEM images of the samples. It is clear that all samples consist of "L"-shaped nanostructures with the lengths of 40-70 μm. It is interesting that the number of "L"-shaped nanostructure increases with the increase of reaction time, and "L"-shaped nanostructures obtained at 24h are more uniform, compared with those at the other reaction times.

3.2 Effect of HNO_3 amount added

The effect of HNO_3 amount added on the samples was also investigated. The amount of 65*wt*% HNO_3 (*x* mL) added was varied, while the other conditions are kept

constant. We find that no products formed when x<10 mL. At x=10 and 15 mL, only a small amount of product can be obtained. Furthermore, the amount of product increases with the amount of HNO_3 added. From Fig. 3a, we can see that all the diffraction peaks are well in accord with standard card (JCPDS no. 41-1426), revealing the formation of phase-pure V_2O_5. Fig. 3(b-d) shows the SEM images of the samples synthesized at different amounts of HNO_3 added. At x=10 mL, the as-prepared sample displays irregular morphology, but with a few of net-like assembles by nanowires (Fig. 3b). At x=15 mL, the broom-like particles form, which are about 70 μm long (Fig. 3c). Fig. 3d shows that the novel "L"-shaped particles have formed, which are about 30-70 μm long. The results above indicate that the amount of HNO_3 added plays a key role in the formation of "L"-shaped V_2O_5, which will be explained in the following section.

3.3 The proposed growth mechanism of "L"-shaped V_2O_5

For layered V_2O_5, it is easy for some guest species (ion, atom or molecules) to insert into the host lattice.[26] Herein, an exfoliating-splitting-assemble model can be used to illustrate the formation of "L"-shaped V_2O_5.[26] Fig. 4 shows the schematic morphological evolution and growth diagram of "L"-shaped V_2O_5. According to above results, we know that a high reaction temperature (180 ℃) is necessary to obtain the well crystalline, "L"-shaped V_2O_5. At the same time, the amount of HNO_3 added plays a key role in the formation of "L"-shaped V_2O_5. In the presence of HNO_3, V_2O_5 can form via hydrolysis and condensation of NH_4VO_3.[26] In our system, all the samples are synthesized in a strong acid environment (pH<0.2), thus, vanadium species mainly exist as the form of VO_2^+.[26] At the initial stage, VO_2^+ species may react with H_2O to form the sheet-like $V_2O_5 \cdot nH_2O$ frameworks. With increasing the

amount of HNO_3, the sheet-like frameworks would be etched slightly to form the meshy V_2O_5 (Fig. 3b and 4a). At more HNO_3, H^+ may insert into the interlayer spaces of $V_2O_5 \cdot nH_2O$ and attack the sheets tempestuously, leading to the formation of broom-like V_2O_5 (Fig. 3c and 4b). With further increasing the amount of HNO_3 added, the sheet-like frameworks is eroded more seriously to form "L"-shaped V_2O_5 (Fig. 3d and 4c). Also according to the time-dependent study, we can find that the nanowires of the side of "L" shape will increase as the time goes on (Fig. 4c-4g). Summarily, "L"-shaped V_2O_5 may form via an etching-exfoliating-splitting-assemble process. It should note that the real formation mechanism needs extensive research.

3.4 Effect of the amount of NaF added

Effect on particle morphology and crystal phase. Fig. 5a shows the scanning electron microscopy (SEM) images of F0. It is clear that without adding *NaF,* the uniform "L"-shaped V_2O_5 has formed, which are about 60-110 μm. Fig. 5b shows that no "L"-shaped particle forms, but only nanowires (F1) can form, which are 200 μm long when the molar ratio of V:F is 1:1. Fig. 5c shows that the length of "L"-shaped particles (F2) is about 3-50 μm at V:F is 1:2. Fig. 5d shows that the morphology of F3 is variety including nanowires, nanoplates and "L"-shape. Further, the effects of NH_4F and NaCl on the sample are shown in Fig. S1 (Supporting Information, SI). It is found that NH_4F has a similar function with NaF, but NaCl can not change the "L" shape of V_2O_5. It is clear that the particle morphology can be changed by F.

The XRD patterns of F0–F3 samples are shown in Fig. 5e. The diffraction peaks at 15.349º, 20.262º, 31.004º and 41.27º can be ascribed to (200), (001), (301) and (600) planes of orthorhombic V_2O_5, respectively. It is clear that (001) peak is strongest for F0, while (301) diffraction peak is strongest for F1 prepared at V:F=1:1

(molar ratio). Furthermore, the intensity ratios of specific diffraction peaks are summarized in Table 1. For F0, the intensity ratios of (001)/(301) and (001)/(200) peaks are 17.23 and 36.96, respectively. This indicates that the (001) plane preferentially grows without adding F. At V/F=1/1, the intensity ratios of (001)/(301) and (001)/(200) peaks are 0.28 and 0.59, respectively. We could believe that F has restrained the growth of (001) plane. At V/F=2, the intensity ratios of (001)/(301) and (001)/(200) peaks are 1.07 and 1.47, respectively. At V/F=4, the intensity ratios of (001)/(301) and (001)/(200) peaks are 0.87 and 1.21, respectively. We could hold that an appropriate amount of F has restrained the growth of (001) plane but accelerate the growth of (301) and (200) plane. We also find that the excess F can not only restrain the growth of (001) plane but also restrain the growth of (301) and (200) planes. Moreover, the growth rate can reach a balance between (001), (301) and (200) planes when V/F is higher than 2. The similar results can be also observed while NH_4F is used (Fig. S2, (SI)).Moreover, a small right shift from 20.34^o to 20.45^o of (001) peak can be observed while adding F (Fig. 5f). It may be caused by the partial substitution of F for O.

HRTEM analysis. Typically, the surface structures of both F0 and F1 were investigated by high-resolution transmission electron microscopy (HRTEM) and selected area electron diffraction (SAED). Fig. 6a shows that the diameters of nanowires are about 150 nm for F0. SAED patterns (the inset of Fig. 6b) reveals the single-crystal nature of V_2O_5. Additionally, the lattice fringe spacing of 0.44 nm well corresponds to (001) plane (0.4379 nm) of orthorhombic V_2O_5, which is in agreement well with XRD patterns (Fig. 5e). The results indicate that the nanowires grow preferentially along the [010] direction and {001} facets are mainly exposed. Our results are similar to the reports.[42,43] For F1 sample, the diameters of nanowires are

around 90-225 nm (Fig. 6c). The single-crystalline nature can also be revealed by SAED patterns (the inset of Fig. 6d). The lattice fringe spacing of 0.57 nm agree well with the (200) plane of orthorhombic V_2O_5, suggesting that the nanowires grow preferentially along [010] direction and {010} facets are mainly exposed. It is obvious that the addition of F has changed the surface of nanowire. Moreover, the lattice fringes of F-doped V_2O_5 become indiscernible indicated by red circle (Fig. 6d), which indicates that some of regions in crystal become disordered. Zhu et al.[44] have attributed this phenomenon to the formed defects. Thus, the oxygen vacancy defects have generated while adding F, which has been further confirmed by photoluminescence (PL) spectra in the latter section.

FT-IR studies. FT-IR spectroscopy is one of the most important means for analyzing the bonding properties of materials. As shown in Fig. 7, the band at 1010-1030 cm^{-1} is recognized as the stretching vibration of V=O.[21] As reported,[45] the bands below 600 cm^{-1} are considered to be the bent V-O-V deformation or edge-sharing V-O stretching. The peaks at 810-850 cm^{-1} and 557-805 cm^{-1} correspond to $[VO_4]^{3-}$ (the coupled vibration between V=O and V-O-V bonds) and F-V bond, respectively.[46] It is strange that there is no characteristic peak at 557-805 cm^{-1} in sample F2 and the nature reason for why the F2 is different from the sample F1 and F3 is still not clear. This needs further study in future. But, it is worth noting that all the samples doped by F show slight band shifts to both higher and lower wavelength. Shao et al. have attributed this shifts to the evolution of V-O bonds.[21] In our study, the evolution of V-O bond may be caused by the substitution of F for O in V_2O_5 lattice, which is similar to F-doped TiO_2.[47] The substitution of F for O has also been confirmed by XRD results, as discussed above (Fig. 5f). The FT-IR spectra of the samples synthesized by using NH_4F and NaCl are shown in Fig. S3 (SI). Comparing Fig. 7 with Fig. S3, we can

infer that the band shift is caused by F, instead of Na, Cl and NH_4.

XPS studies. The XPS spectra of F0, F1, F2 and F3 samples are shown in Fig. 8. Fig. 8a shows their survey spectra and Fig. 8b shows V 2p3/2, V 2p1/2 and O 1s spectra of the samples. The peaks at about 517.6 and 525 eV corresponds to the V (5+) species.[32,48-50] O 1s peak at about 530.2 eV corresponds to O^{2-} in V_2O_5 lattice.[50-52] In Fig. 8c, two peaks at about 684 and 688.5 eV can correspond to F 1s for F1, F2 and F3.[53] The F element atomic concentrations of the samples are shown in Table S1 (SI). Table S1 shows that the concentration of F element in F1, F2 and F3 are 1.71, 1.42 and 1.69 *at*%), thus resulting in the weak XPS signal of F 1s. This indicating that only fairly small amount of F^- can substitute for O^{2-} in the lattice of V_2O_5.

Optical properties. Fig. 9 shows the ultraviolet-visible diffuse reflectance spectra (UV-DRS) of the samples. According to the previous report,[54] the energy band gap of semiconductor also can be calculated by the following equation:

$$E_g = 1240/\lambda \quad (1)$$

where E_g is the band gap (eV), λ is the wavelength (nm) of absorption edge in the spectrum. The band gaps are about 1.93, 1.97, 1.91 and 2.09 eV for F0, F1, F2 and F3 samples, respectively. It has been reported that the diameter of 1D V_2O_5 nanostructure has an great influence on band gap values.[55,56] According to previous report,[57] V_2O_5 is a semiconductor with both direct and indirect energy band gap. Herein, our calculation results show that V_2O_5 is an indirect transition semiconductor, as shown in Fig. S4 (SI).

Additionally, the optical band gap of V_2O_5 for direct and indirect band gap transition can also be estimated by Tauc equation (Eq. (2)) as follows.[58]

$$\alpha h\nu = K(h\nu - E_g)^{n/2} \quad (2)$$

where α, ν, h, K, and E_g represent absorption coefficient, photon frequency, Planck's

constant, proportionality constant and optical band gap of a semiconductor, respectively; *n* is dependent on the optical transition type of a semiconductor, with a value of 1 or 4.[59] As reported,[59,60] the square of absorption coefficient is linear with a direct optical transition energy in the absorption edge region of a semiconductor, whereas the square root of absorption coefficient is linear with an indirect optical transition energy.[60] Thus, $n = 1$ represents a direct absorption and $n = 4$ represents an indirect absorption of semiconductor.[59-61] According to the plot of $(\alpha hv)^{1/2}$ against hv (Fig. 9b), we can observed that the indirect band gaps of F0, F1, F2 and F3 samples are about 1.91 eV, 1.94 eV, 1.87 eV and 2.04 eV, respectively, which are smaller than the intrinsic band gap of 2.2-2.4 eV.[62,63] From the plot of $(\alpha hv)^2$ against hv (Fig. 9c), the direct band gaps of F0, F1, F2 and F3 are determined to be 2.18. 2.2, 2.15 and 2.21 eV, respectively. Those results show that the indirect band gap of the samples are a slightly smaller than the direct band gap values, which is similar to the former reports.[55,57] From the above results, we can find that the indirect band gap is more suitable for V_2O_5 synthesized in this work. The band gaps of V_2O_5 synthesized in our system are slightly smaller than reported,[55, 57] which indicates that the V_2O_5 samples synthesized in our system can improve the light utilization.

Photoluminescence (PL) spectroscopy analysis. The photoluminescence (PL) spectroscopy has been widely used to investigate the optical properties and the recombination rate of electron and hole pairs of semiconductor.[48,63,64] Thus, we have measured PL spectra of the samples with the excitation wavelength of 260 nm (Fig. 10). The broad emission peak observed at about 424 nm can be attribute to the recombination of self-trapped excitons derived from the charge transition between valence band (O 2p) and conduction band (V 3d) excited from V_2O_5 species.[48,63,65] Additionally, the other emission bands can be caused by defects,[63,66] namely, oxygen

vacancy. It is widely accepted that PL emission peak intensity is corresponding to the recombination efficiency of the excited electron and hole pairs.[48] It is clear that the recombination rate of electron and hole pairs of F-doped V_2O_5 is faster than the pure V_2O_5 sample. This also indicate that more defects are produced due to doping of F.[53,67,68]

3.5 Calculation results.

Furthermore, we have calculated the surface energies of (001), (010) (100), (110) and (301) facets, as shown in Fig. 11. Surface free energy (γ) is calculated by the following formulae:[69]

$$\gamma = (E_{Slab} - N * E_{Bulk})/2A \quad (3)$$

where E_{slab} is the total energy of the slab, E_{Bulk} is the energy per unit of material, N is the ratio of total number contained in the super cell of unit slab and V_2O_5, and A is the surface area of slab. The surface energies of (001), (010), (100), (110) and (301) facets are 0.099, 8.936, 4.502, 2.669 and 6.384 J/m^2, respectively; demonstrating that the surface energy of (001) facet is much smaller than those of the others, which is well agree with the other report.[70] Sayle et al.[70] have also reported that the surface energy of {001} planes is obviously smaller than those of the others. On base of analyses results above, the high-energy {010} facets exposed may favor to the performance improvement.

3.6 Adsorption of MB

Adsorption performances. It is well known that the adsorption rate, adsorption efficiency and adsorption capacity are three important parameters, which can be

reflected by adsorption kinetics. The absorption amount (Q_t) and removal percentage (R%) are calculated by the following equations, respectively.[12,14]

$$Q_t = (C_0 - C_t)\ V/W \quad (4)$$

$$R\% = C_0 - C_t/C_0 * 100 \quad (5)$$

where Q_t is the adsorption quantity (mg/g) of adsorbate at t min, C_0 is the initial concentration (mg/L) of adsorbate, C_t is the concentration (mg/L) of adsorbate at t min, W and V are the weight of absorbent (g) and the volume (L) of adsorbate solution, respectively; R% is the removal percentage (%).

The adsorption kinetics of MB over the samples have been investigated by using pseudo first order kinetic model (Eq. (6)) and pseudo second order kinetic model (Eq. (7)), expressed as the following equation:[11,71]

$$\ln(Q_e - Q_t) = \ln Q_e - K_1\ t \quad (6)$$

$$t/Q_t = 1/K_2 Q_e^2 + t/Q_e \quad (7)$$

where K_1 and K_2 are the rate constants of pseudo first order (L/min) and pseudo second order adsorption (g/mg min), respectively. The kinetic parameters are calculated on base of the plots of $\ln(Q_e\text{-}Q_t)$ *versus* t and t/Q_t *versus* t.

Fig. 12 shows the effect of contact time on the removal efficiency of MB (20 mg/L) over the samples. From Fig. 12a, we can see that after 35 min, an adsorption equilibrium can reach over F1 and F2 and an adsorption equilibrium reach over F3 after 125 min; but an absorption equilibrium can reach over F0 at 445 min. From Fig. 12b, we can find that all the samples show high removal efficiencies for MB. When absorption equilibriums are reached, the removal percentage of MB over these samples decrease in the following order: F1 (99.7%) > F2 (96.5%) > F3 (94.6%) > F0

(83%). Among them, interestingly, the highest removal percentage (99.7%) of MB can reach over F1 , which is much higher than that over F0. Their differences may be attributed to the following reasons: Firstly, Table 2 shows that the surface areas of F1, F2 and F3 are 2.1, 1.3 and 1.6 times larger than that of F0, respectively. The improved surface area may provide more absorption sites, so the absorption capacities of F1, F2 and F3 are higher than that of F0. Secondly, the calculation results show that the surface energy of (010) facets is higher than that of {001} facets. Herein, the high-energy {010} facets exposed may be another important factor for the improved adsorption capacity of F1. What is more, the present F is conductive to the absorption of cationic MB dye through an electrostatic attraction force.

To evaluate the absorption kinetics of MB over the samples, the pseudo-first-order and pseudo-second-order are applied to analyze our experimental data.[11] The pseudo-first-order curves of MB over samples are shown in Fig. 12c and the relative parameters are summarized in Table 3. From Table 3, we can see that the correlation coefficients (R_1^2) of F0, F1, F2 and F3 are 0.85, 0.57, 0.29 and 0.47, respectively. The low correlation coefficients suggest that the adsorption of MB over the samples poorly fit with pseudo-first-order model. The plots of t/Q_t *versus* t (pseudo-second-order curves) are shown in Fig. 12d and the relative parameters are also listed in Table 3. As is shown in Table 3, the correlation coefficients (R_2^2) values are all higher than 0.95, illustrating that the adsorption of MB over all the samples fit well with pseudo-second-order kinetic model. To conclude, the adsorption of MB over the samples are mainly controlled by chemisorptions, rather than by physical

adsorption.

Further, in order to understand the influence of initial concentration of MB on adsorption kinetics, we have changed the concentration of MB from 10 to 100 mg/L. As shown in Fig. 13a, the maximum absorption amount of MB over F1 is observed at 35 min at 10 and 20 mg/L of MB. When the initial concentration of MB is increased to 50 and 100 mg/L, a long time (135 min) is needed to reach the equilibrium. From Fig. 13b, we can also observe that the absorption rates are rather fast at the initial stage and then become slow gradually; and the removal percentages are above 97% when the initial concentration of MB is lower than 100 mg/L.

The pseudo-first-order and pseudo-second-order are also applied to analyze the influence of initial MB concentration. The plots of $\ln(Q_e-Q_t)$ and t/Q_t *versus* t are shown in Fig. 13c and 13d, respectively; and Table 4 presents the relative parameters. It can be found that at 10, 20, 50 and 100 mg/L of MB, the correlation coefficients (R_1^2) are 0.07, 0.57, 0.86 and 0.97, respectively. The low correlation coefficients suggest that the adsorption of MB over F1 poorly fit with pseudo-first-order model. But, the correlation coefficients (R_2^2) are all higher than 0.99, demonstrating that the adsorption of MB fits well with pseudo-second-order kinetics. To conclude, the initial concentration of MB has no influence on the absorption kinetic over F1.

Adsorption mechanism. Langmuir and Freundlich isotherms are often used to describe the adsorption mechanism. Langmuir adsorption isotherm is based on the assumption that adsorption occurs on a homogeneous solid surface; while Freundlich adsorption isotherm is based on the assumption over a heterogeneous solid surface.

The adsorption isotherms can be expressed in the following equations (8) and (9), respectively:[72,73]

$$C_e/Q_e = 1/(K_L * Q_m) + C_e/Q_m \quad (8)$$

$$\log Q_e = \log K_F + (\log C_e)/n \quad (9)$$

where Q_e is the adsorption amount (mg/g) at equilibrium, C_e is the equilibrium concentration (mg/L) of adsorbate, K_L is a constant relative to the adsorption energy (L/mg), Q_m is Langmuir monolayer adsorption amount (mg/g), K_F is an indicator of adsorption capacity, and n is the adsorption intensity.

From Fig. 14, we can see that the adsorption isotherm of MB over F1 can be well fitted to a Langmuir model, rather than a Freundlich model. This indicates that a monolayer adsorption of MB occurs over F1, rather than multilayer. This result is similar to the adsorption of MB over graphene, as reported by Shen et al.[74]

4. Conclusion

Novel "L"-shaped V_2O_5 nanostructures can be prepared by a simple hydrothermal method. Moreover, doping of fluorine not only increases the oxygen vacancy, but also makes the higher energy surface ({010} facets) exposed, compared with "L" shaped V_2O_5 with low-energy {001} facets exposed. The fluorine has improved the adsorption capacity greatly. Further study will be carried out to investigate their photocatalytic and electrochemical performances.

Acknowledgments

This work is financially supported by National Science Foundation of China (21377060, 21103049), Six Talent Climax Foundation of Jiangsu (20100292), Jiangsu Science Foundation of China (BK2012862), Jiangsu Province of Academic Scientific Research Industrialization Projects (JHB2012-10), The Project of Foreign Culture and Education expert (N0502001003), Jiangsu province of Key Environmental protection projects (2012028), Teaching Reform Project to Enhance the Practice Innovation of NUIST-2013 (N1885013014), Support Program for Undergraduate Dissertation of NUIST-2013 (N1085002008), A Project Funded by the Priority Academic Program Development of Jiangsu Higher Education Institutions (PAPD), and Jiangsu Province Innovation Platform for Superiority Subject of Environmental Science and Engineering, “333” Outstanding Youth Scientist Foundation of Jiangsu (2011-2015), the Project Sponsored by SRF for ROCS, SEM (2013S002).

References

(1) G. L. Dotto, J. M. Moura, T. R. S. Cadaval and L. A. A. Pinto, *Chem Eng. J.,* 2013, **214**, 8-16.

(2) M. M. Ayad and A. Abu El-Nasr, *J Phys Chem C.,* 2010, **114**, 14377-14383.

(3) S. A. Ong, E. Toorisaka, M. Hirata and T. Hano, *J. Hazard Mater.,* 2005, **124**, 88-94.

(4) P. Luo, Y. Zhao, B. Zhang, J. Liu, Y. Yang and J. Liu, *Water Res.,* 2010, **44**, 1489-1497.

(5) L. Marçal, E. H. de Faria, E. J. Nassar, R. Trujillano, N. Martín, M. A. Vicente, V. Rives, A. Gil, S. A. Korili and K. J. Ciuffi, *ACS Appl. Mater. Inter.,* 2015. **7**, 10853−10862

(6) D. Kołodyńska, R. Wnętrzak, J. Leahy, M. Hayes, W. Kwapiński and Z. Hubicki, *Chem Eng. J.,* 2012, **197**, 295-305.

(7) O. R. Harvey, B. E. Herbert, R. D. Rhue and L. J. Kuo, *Environ. Sci. Technol,.* 2011, **45**, 5550-5556.

(8) S. Yang, J. Hu, C. Chen, D. Shao and X. Wang, *Environ. Sci. Technol.,* 2011**, 45**, 3621-3627.

(9) R. Tovar-Gomez, D. Rivera-Ramírez, V. Hernandez-Montoya, A.Bonilla-Petriciolet and C. Durán-Valle, *J. Hazard Mater.,* 2012, **199**, 290-300.

(10)J. Luo, X. Luo, J. Crittenden, J. Qu, Y. Bai, Y. Peng and J. Li, *Environ. Sci. Technol.,* 2015, **49**, 11115-11124.

(11) Z. Wu, H. Zhong, X. Yuan, H. Wang, L. Wang, X. Chen, G. Zeng and Y. Wu, *Water Res.,* 2014, **67**, 330-344.

(12) Y. Shen and Q. Fang, B. Chen, *Environ. Sci. Technol.,* 2014, **49**, 67-84.

(13) C. X. Gui, Q. Q. Wang, S. M. Hao, J. Qu, P. P. Huang, C. Y. Cao, W. G. Song and Z. Z. Yu, *ACS Appl. Mater. Inter.,* 2014, **6**, 14653-14659.

(14) B. J. Zhu, X. Y. Yu, Y. Jia, F. M. Peng, B. Sun, M. Y. Zhang, T. Luo, J. H. Liu and X. J. Huang, *J. Phys. Chem. C,* 2012, **116**, 8601-8607.

(15) W. Wei, P. Gao, J. Xie, S. Zong, H. Cui and X. Yue, *J. Solid State. Chem.,* 2013, **204**, 305-313.

(16) T. Shen, J. Luo, S. Zhang and X. Luo, *J. Environ. Chem. Eng.,* 2014, **3**, 1372-1383.

(17) U. Tritschler, I. Zlotnikov, P. Zaslansky, P. Fratzl, H. Schlaad and H. Cölfen, *ACS Nano.,* 2014, **8**, 5089-5104.

(18) C. T. Yavuz, J. Mayo, W. Y. William, A. Prakash, J. C. Falkner, S. Yean, L. Cong, H. J. Shipley, A. Kan and M. Tomson, *Science,* 2006**, 314**, 964-967.

(19) F. Zhou, X. Zhao, C. Yuan and L. Li, *Crystal. Growth Des.,* 2007, **8**, 723-727.

(20) R. André, F. Natálio, M. Humanes, J. Leppin, K. Heinze, R. Wever, H. C. Schröder, W. E. Müller and W. Tremel, *Adv. Funct. Mater.,* 2011, **21**, 501-509.

(21) L. Shao, K. Wu, X. Lin, M. Shui, R. Ma, D. Wang, N. Long, Y. Ren and J. Shu, *Ceram. Int.,* 2014, **40**, 6115-6125.

(22) S. D. Perera, B. Patel, J. Bonso, M. Grunewald, J. P. Ferraris and K. J. Balkus Jr *ACS Appl. Mater. Inter.* 2011, **3**, 4512-4517.

(23) A. M. Glushenkov, V. I. Stukachev, M. F. Hassan, G. G. Kuvshinov, H. K. Liu and Y. Chen, *Crystal. Growth Des.,* 2008, **8**, 3661-3665.

(24) C. Diaz-Guerra and J. Piqueras, *Crystal. Growth Des.,* 2008, **8**, 1031-1034.

(25) S. Shi, M. Cao, X. He and H. Xie, *Crystal. Growth Des.,* 2007, **7**, 1893-1897.

(26) H. S. Lim, D. Kwak, D. Y. Lee, S. G. Lee and K. Cho, *J. Am. Chem. Soc.* 2007, **129**, 4128-4129.

(27) M. R. Parida, C. Vijayan, C. S. Rout, C. S. Sandeep, R. Philip and P. Deshmukh, *J Phys. Chem. C.,* 2010, **115**, 112-117.

(28) X.Zhang, M. Wu, S. Gao, Y. Xu, X. Cheng, H. Zhao and L. Huo, *Mater. Res. Bull.,* 2014, **60**, 659-664.

(29) Y. Wu, H. Luo, H. Wang, C. Wang, J. Zhang and Z. Zhang, *J.Colloid. Interf. Sci.,* 2013, **394**, 183-191.

(30) M. Shanmugam, A. Alsalme, A. Alghamdi and R. Jayavel, *ACS Appl. Mater. Inter.,* 2015, **7**, 14905-14911.

(31) A.Sakunthala, M. Reddy, S. Selvasekarapandian, B. Chowdari and P. C. Selvin, *Energ. Environ. Sci.,* 2011, **4**, 1712-1725.

(32) H. Yu, X. Rui, H. Tan, J. Chen, X. Huang, C. Xu, W. Liu, Y. Denis, H. H. Hng and H. E. Hoster, *Nanoscale,* 2013, **5**, 4937-4943.

(33) Y. Xu, M. Dunwell, L. Fei, E. Fu, Q. Lin, B. Patterson, B. Yuan, S. Deng, P. Andersen and H. Luo, *ACS Appl. Mater. Inter.,* 2014, **6**, 20408-20413.

(34) R. Gao, D. Zhang, X. Liu, L. Shi, P. Maitarad, H. Li and W. Cao, *Catal. Sci. Technol.,* 2013, **3**, 191-199.

(35) F. Giraud, J. Couble, C. Geantet, N. Guilhaume, E. Puzenat, S. Gros, and D. Bianchi, *J. Phys. Chem. C,* 2015, **119**, 16089−16105.

(36) A. Q. Pan, H. B. Wu, L. Zhang and X. W. Lou, *Energy Environ. Sci.,* 2013, **6**, 1476-1479.

(37) S. Wang, Z. Lu, D. Wang, C. Li, C. Chen and Y. Yin, *J. Mater. Chem.,* 2011, **21**, 6365-6369.

(38) S. Yuan, Y. B. Liu, D. Xu, D. L. Ma, S. Wang, X. H. Yang and X. B. Zhang, *Adv. Sci.,* 2015, 2, 1400018-140024.

(39) H. G. Wang, D. Ma, X. L. Huang, Y. Huang and X. B. Zhang, *Sci. Rep.,* 2012, **2**, 701-709.

(40) X. L. Huang, R. Z. Wang, D. Xu, Z. L. Wang, H. G. Wang, J. J. Xu and X. B. Zhang, *Adv. Funct. Mater.* 2013, **23**, 4345–4353.

(41) X. Zhao, L. Huang, H. Li, H. Hu, J. Han, L. Shi and D. Zhang, *Chinese J Catal,* 2015, **36**, 1886–1899.

(42) P. Ragupathy, S. Shivakumara, H. N. Vasan and N. Munichandraiah, *J. Phys. Chem. C,* 2008, **112**, 16700-16707.

(43) Jr, W. Avansi C. Ribeiro, E. R. Leite and V. R. Mastelaro, *Crystal Growth and Des.*, 2009, **9**, 3626-3631.

(44) D. Chen, Z. Wang, T. Ren, H. Ding, W. Yao, R. Zong and Y. Zhu, *J. Phys. Chem. C,* 2014, **118***,* 15300–15307.

(45) E. Almeida, M. Abbate and J. Rosolen, *J. Power Sources,* 2002, **112**, 290-293.

(46) E. A. Ponzio, T. M. Benedetti and R. M. Torresi, *Electrochim. Acta.,* 2007, **52**, 4419-4427.

(47) W. Zhao, Q. Zhong, T. Zhang and Y. Pan, *RSC Adv.,* 2012, **2**, 7906-7914.

(48) R. Suresh, K. Giribabu, R. Manigandan, S. Munusamy, S. P. Kumar, S. Muthamizh, A. Stephen and V. Narayanan, *J. Alloy. Compd,*. 2014, **598**, 151-160.

(49) C. Zou, Y. Rao, A. Alyamani, W. Chu, M. Chen, D. A. Patterson, E. A. Emanuelsson and W. Gao, *Langmuir,* 2010, **26**, 11615-11620.

(50) J. Sun, X. Li, Q. Zhao, J. Ke and D. Zhang, *The J. Phys. Chem. C,* 2014, **118**, 10113-10121.

(51) Y. Suchorski, L. Rihko-Struckmann, F. Klose, Y. Ye, M. Alandjiyska, K. Sundmacher and H. Weiss, *Appl. Surf. Sci.,* 2005, **249**, 231-237.

(52) S. Karamat, R. Rawat, P. Lee, T. Tan, R. Ramanujan and W. Zhou, *Appl. Surf. Sci.,* 2010, **256**, 2309-2314.

(53) J. C. Yu, J. Yu, W. Ho, Z. Jiang and L. Zhang, *Chem. Mater.,* 2002, **14**, 3808-3816.

(54) J. Senthilnathan and L. Philip, *Chem Eng. J.,* 2010, **161**, 83-92.

(55) H. Howari and S. Mohamed, *J. Phys. Chem. Solids.,* 2013, **74**, 630-634.

(56) V. Ivanovskaya, A. Enyashin, A. Sofronov, Y. N. Makurin, N. Medvedeva and A. Ivanovskii, *Solid State Commun.,* 2003, **126**, 489-493.

(57) J. Parker, D. Lam, Y. N. Xu and W. Ching, *Phys Rev. B.,* 1990, **42**, 5289.

(58) J. Tauc, Springer: 1974, 159-220.

(59) J. Tauc, R. Grigorovici and A. Vancu, *Phys Status solidi B.,* 1966, **15**, 627-637.

(60) H. Tian, F. Teng, J. Xu, S. Lou, N. Li, Y. Zhao and M.Chen, *Sci. Rep.,* 2015, **5**, 7770.

(61) S. Sun, W. Wang, L. Zhang, L. Zhou, W. Yin and M. Shang, *Sci. Technol.,* 2009, **43**, 2005-2010.

(62) Y. Wang, Z. Li, X. Sheng and Z. Zhang, *J. Chem. Phys.,* 2007, **126**, 164701.

(63) R. Abazari, S. Sanati and L. A. Saghatforoush, *Chem Eng. J.,* 2014, **236**, 82-90.

(64) H. Yamashita, Y. Ichihashi, S. G. Zhang, Y. Matsumura, Y. Souma, T. Tatsumi and M. Anpo, *Appl. Surf. Sci.,* 1997, **121**, 305-309.

(65) H. Tang, K. Prasad, R. Sanjines, P. Schmid and F. Levy, *J. Appl. Phys.,* 1994, **75**, 2042-2047.

(66) M. Kang, E. Oh, I. Kim, S. W. Kim, J. W. Ryu and Y. G. Kim, *Curr. Appl. Phys.,* 2012**, 12**, 489-493.

(67) X. Li and F. Li, *Environ. Sci. Technol.,* 2001, **35**, 2381-2387.

(68) X. Li, F. Li, C. Yang and W. Ge, *J. Photoch. Photobio. A,* 2001, **141**, 209-217.

(69) B. Romero, S. Bruque, M. A. Aranda and J. E. Iglesias, *Inorg. Chem.*, 1994, **33**, 1869-1874.

(70) D. C. Sayle, D. H. Gay, A. L. Rohl, C. R. A. Catlow, J. H. Harding, M. A. Perrin and P. Nortier, *J. Mater. Chem.*, 1996, **6**, 653-660.

(71) Y. Önal, C. Akmil-Başar, D. Eren, Ç. Sarıcı-Özdemir and T. Depci, *J. Hazard Mater.,* 2006, **128**, 150-157.

(72) I. Langmuir, *J. Am. Chem. Soc.,* 1916, **38**, 2221-2295.

(73) H. Freundlich, *J. Phys. Chem,* 1906, **57**, e470.

(74) Y. Shen and B. Chen, *Environ. Sci. Technol.,*2015, **49**, 7364−7372.

List legends of Tables and Figs.

Table 1

Peak intensity ratios of (001)/(301) and (001)/(200) of the samples

Crystal facet	(001)/(200)	(001)/(301)
Stand card	3.03	0.96
F0	36.96	17.23
F1	0.59	0.28
F2	1.47	1.07
F3	1.21	0.87

Table 2

Surface areas of the samples

Sample	BET surface area (m^2 g^{-1})	Pore volume (cm^3 g^{-1})	Pore diameter (nm)
V_2O_5(400 °C, 2h)	5.8	0.099	3.422
F0	17.7	0.063	6.554
F1	37.7	0.080	6.562
F2	22.7	0.083	3.056
F3	28.3	0.080	3.057

Notes: BET surface area, calculated by the Brunauer–Emmett–Teller (BET) method; Pore volume and Pore diameter, calculated by the Barret–Joyner–Halender (BJH) method.

Table 3

Adsorption kinetics parameters of MB over V_2O_5 samples

Adsorbate	C_0 (mg/L)	Samples	$Q_{e,exp}$ (mg/g)	Pseudo-first-order model		Pseudo-second-order model	
				$K_1(min^{-1})$	R_1^2	$K_2(g\ mg^{-1}\ min^{-1})$	R_2^2
MB	20	F0	13.3	0.0108	0.85	0.0652	0.95
		F1	16.0	0.0088	0.57	0.0625	0.99
		F2	15.4	0.0069	0.29	0.0645	0.99
		F3	15.1	0.0102	0.47	0.0617	0.99

Notes: C_0 is the initial concentration (mg/L) of MB dye solution; $Q_{e,exp}$ presents the adsorption capacity (mg/g) at the equilibrium; K_1 and K_2 are the rate constants of pseudo first order (L/min) and the rate constant of the pseudo second order adsorption (g/mg min), respectively; R^2 is the correlation coefficients.

Table 4

Adsorption kinetics parameters over F1 sample at different initial concentrations of MB

Adsorbate	C_0 (mg/L)	Samples	Qe,exp (mg/g)	Pseudo-first-order model		Pseudo-second-order model	
				$K_1(min^{-1})$	R_1^2	$K_2(g\ mg^{-1}\ min^{-1})$	R_2^2
MB	10	F1	7.9	0.0019	0.07	0.125	0.99
	20		16.0	0.0088	0.57	0.0625	0.99
	50		38.9	0.00157	0.86	0.0244	0.99
	100		56.5	0.0192	0.97	0.0167	0.99

Fig. 1

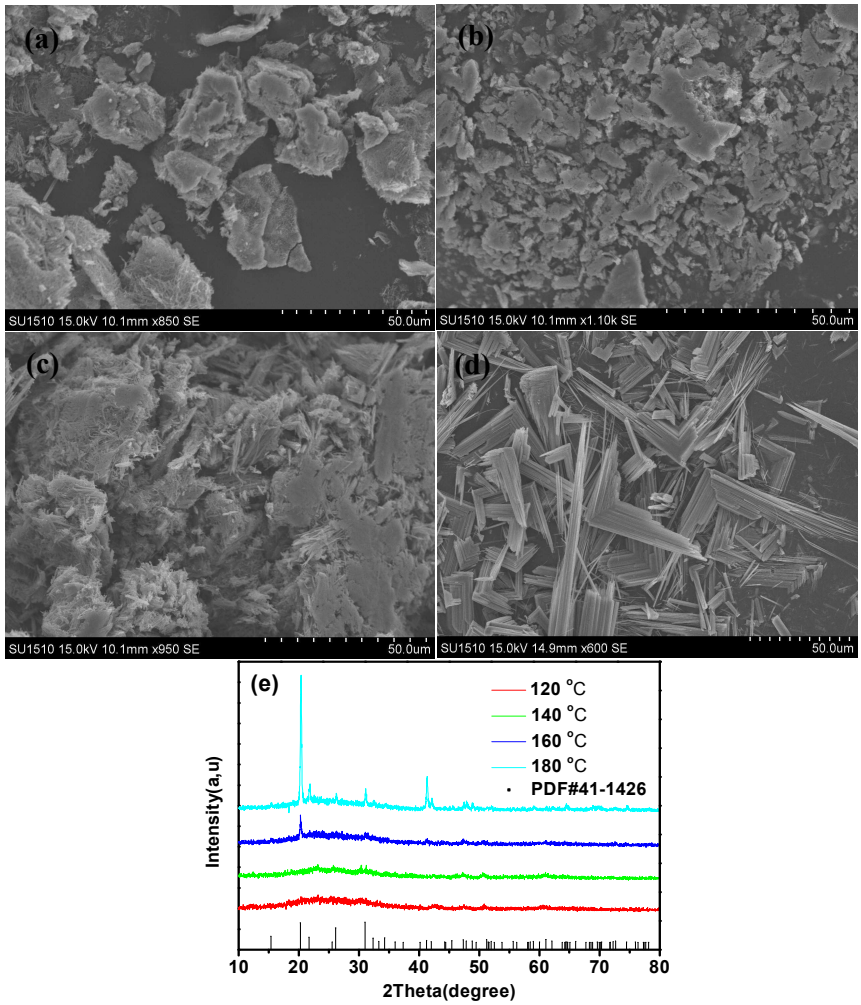

Fig. 1 SEM images (a-d) and XRD patterns (e) of the samples synthesized at different reaction temperature (a) 120 °C; (b) 140 °C; (c) 160 °C; (d) 180 °C.

Fig. 2

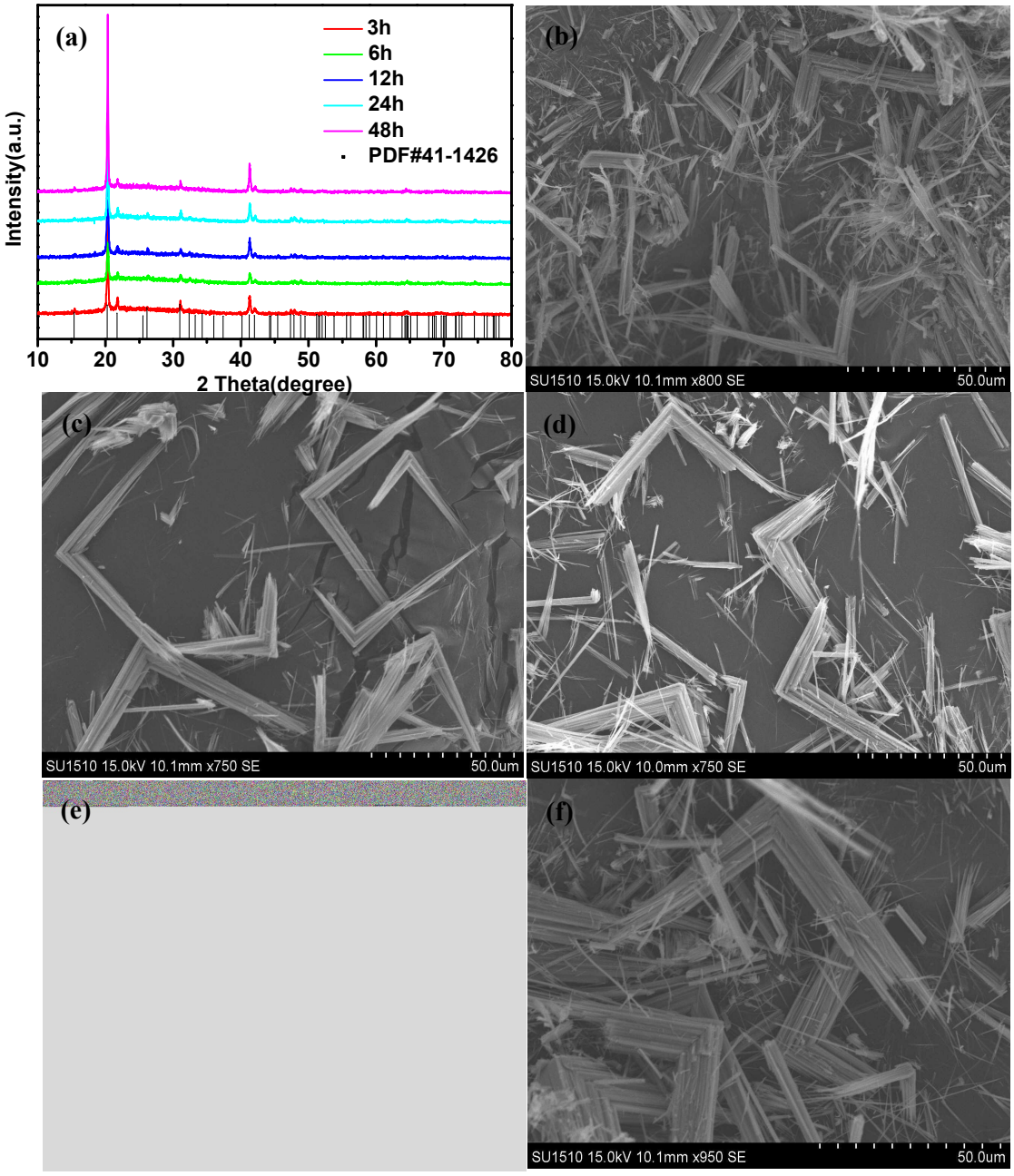

Fig. 2 XRD patterns (a) and SEM images (b-f) of the samples at 180 °C, 20 mL HNO_3 (65 *Wt.*%): (b) 3 h ;(c) 6 h; (d) 12 h; (e) 24 h; (f) 48 h.

Fig. 3

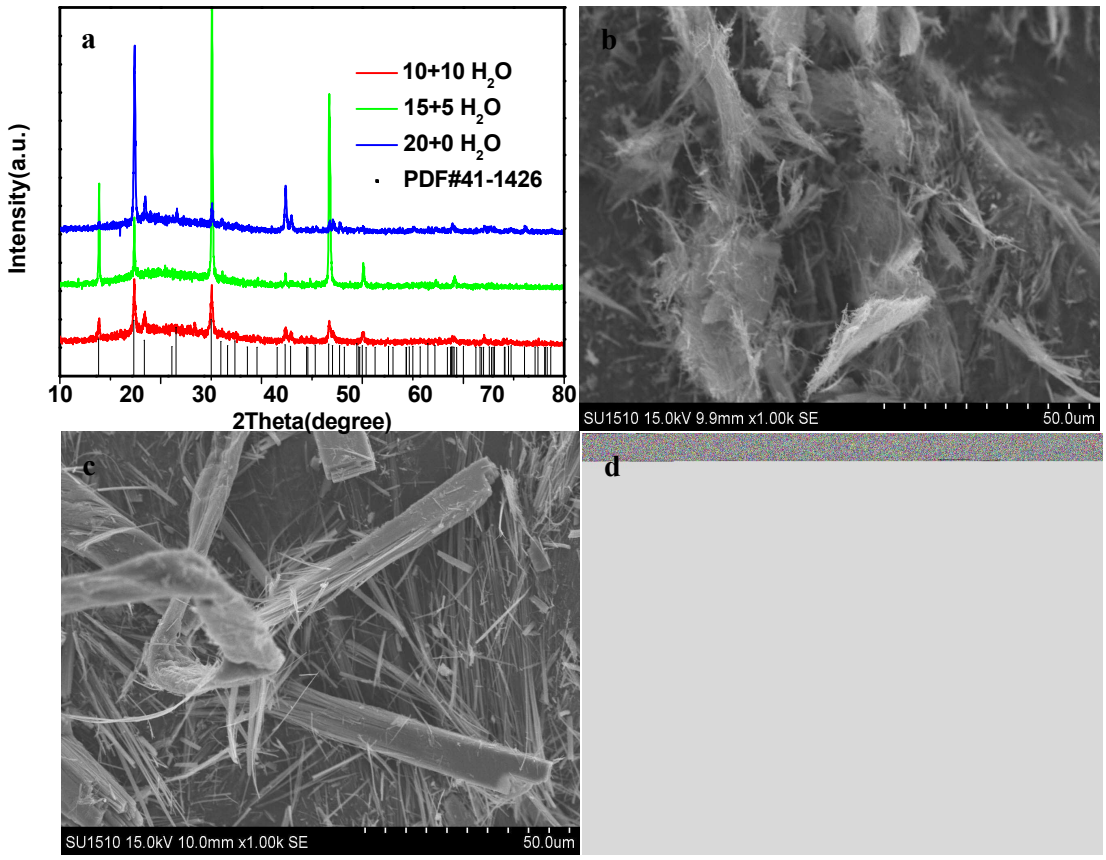

Fig. 3 XRD patterns (a) and SEM images (b-d) of the samples at 180 °C for 24h with different HNO_3 (65*wt*%) amounts; (b) 10 mL HNO_3 + 10mL H_2O; (c) 15 mL HNO_3 + 5mL H_2O; (d) 20 mL HNO_3 + 0mL H_2O.

Fig. 4

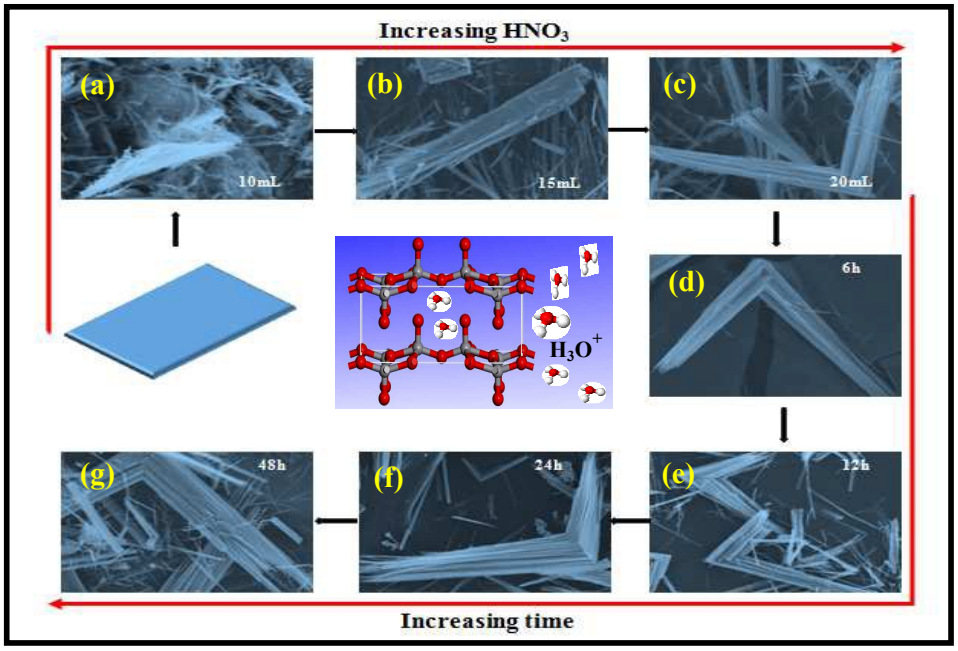

Fig. 4 Schematic diagram for the morphological evolution and growth of V_2O_5 "L" shape (180 °C).

Fig. 5

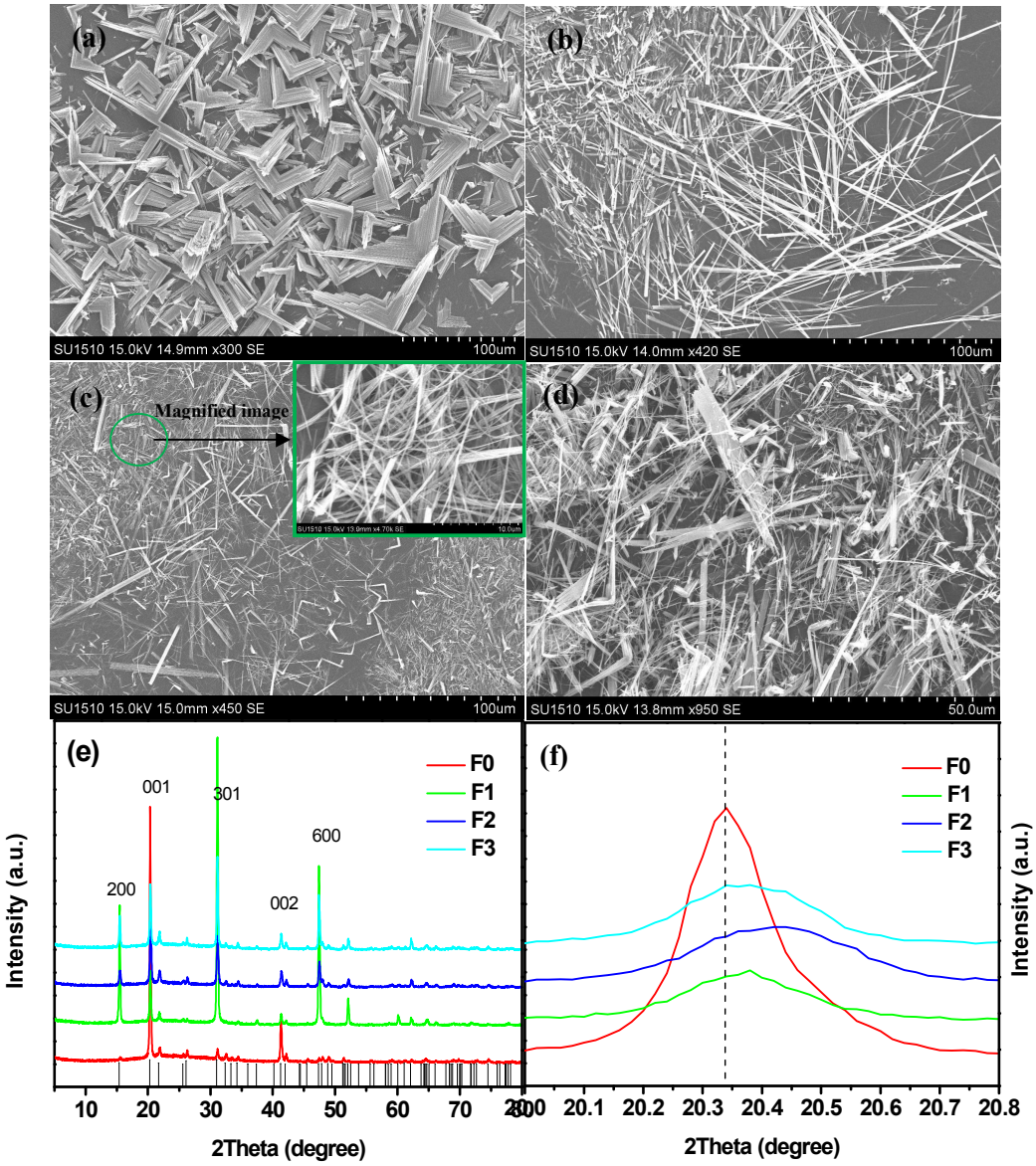

Fig. 5 SEM micrographs (a-d) and X-ray diffraction (XRD) patterns of the samples a) F0; b) F1; c) F2; d) F3; e) XRD at a scanning rate of 2 ^{o}/min; f) The magnified XRD.

Fig. 6

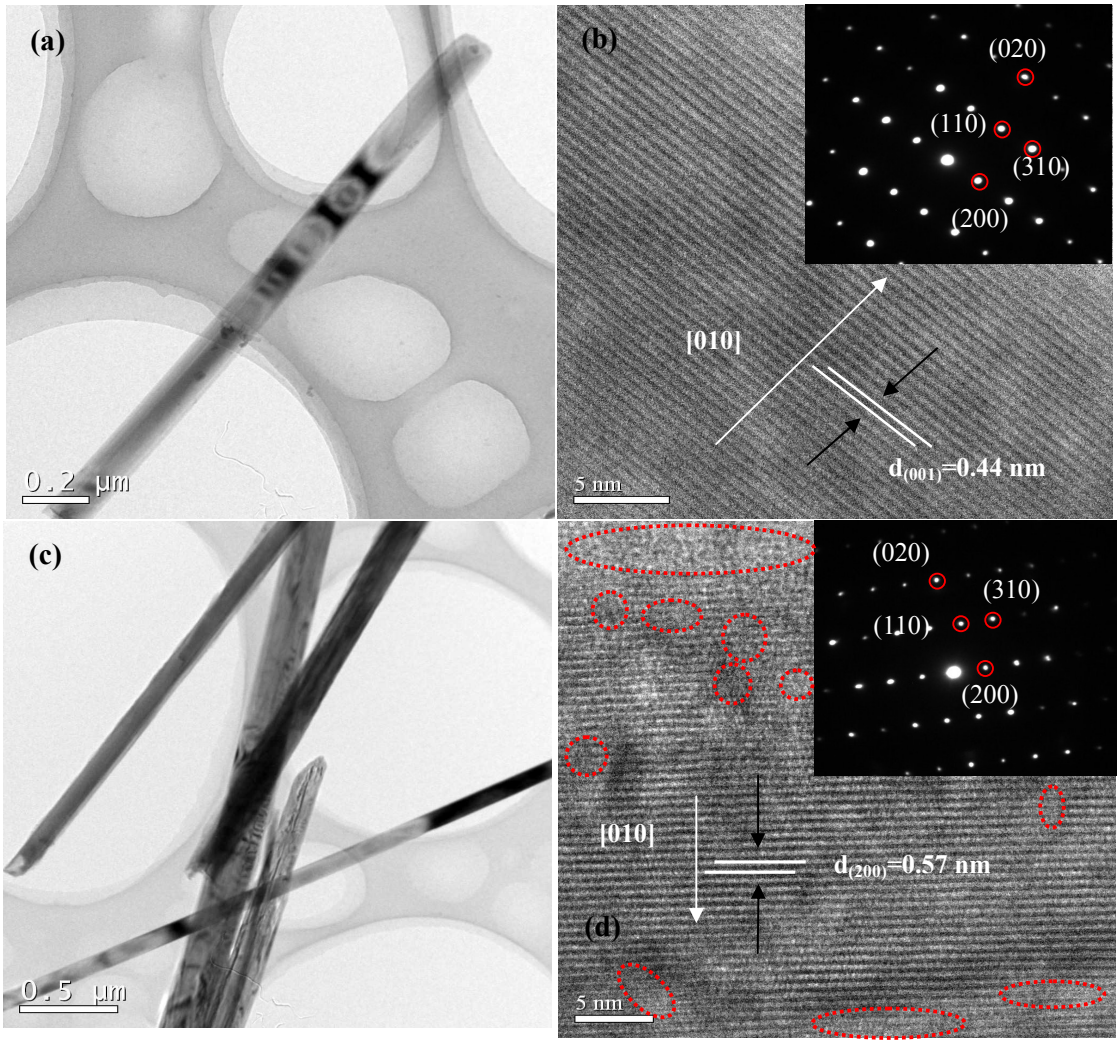

Fig. 6 (a,c) HRTEM images and (b,d) lattice fringe images and SAED patterns (recorded in [001] zone axis) of the samples (a,b) F0; (c,d) F1; the red circle presents the indiscernible lattice fringes.

Fig. 7

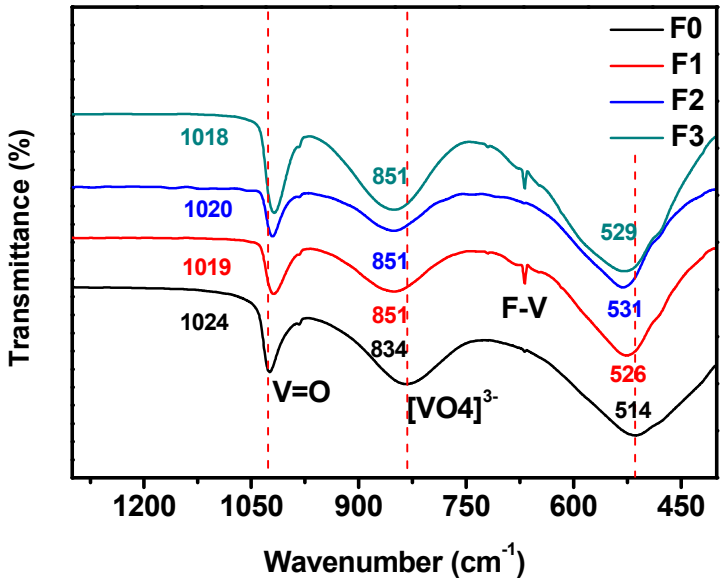

Fig. 7 FT-IR spectra of samples F0, F1, F2 and F3.

Fig. 8

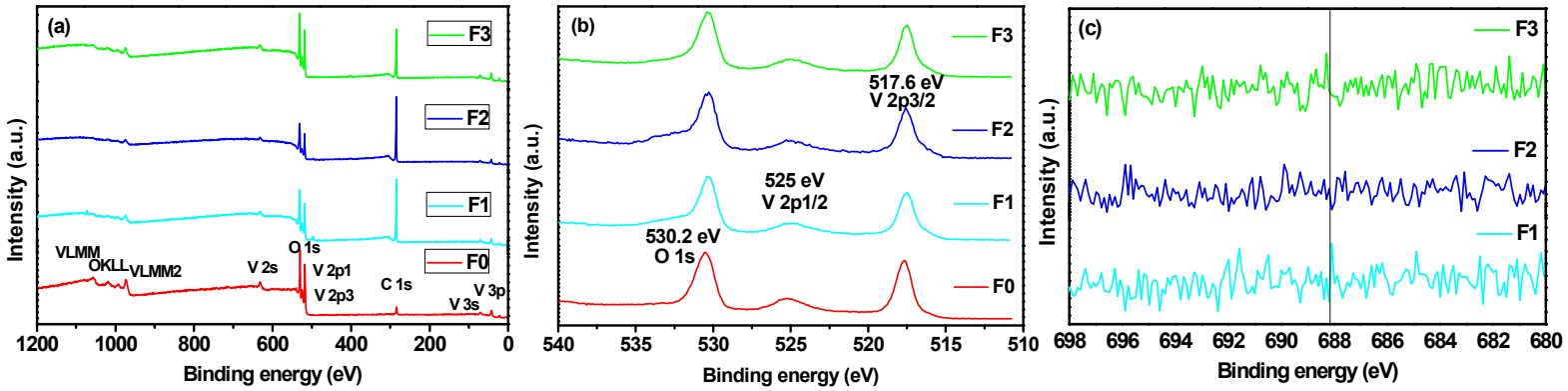

Fig. 8 XPS spectra of samples (a) Survey spectra, (b) O 1s and V 2p spectra, (c) F 1s spectra.

Fig. 9

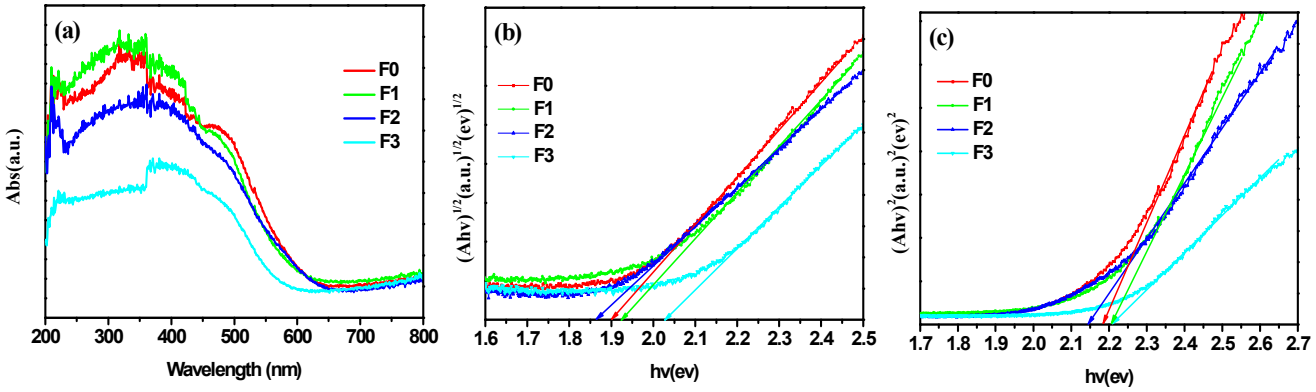

Fig. 9 UV/Vis diffuse reflectance spectra of the samples.

Fig. 10

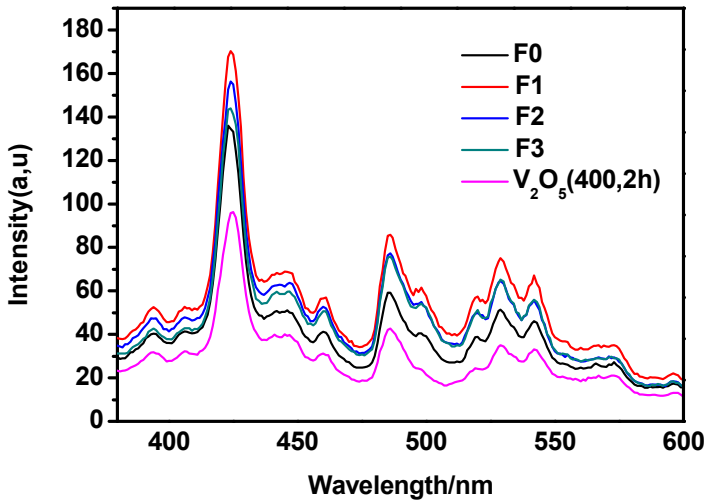

Fig. 10 Photoluminescence spectra of the samples under 260 nm excitation taken at room-temperature.

Fig. 11

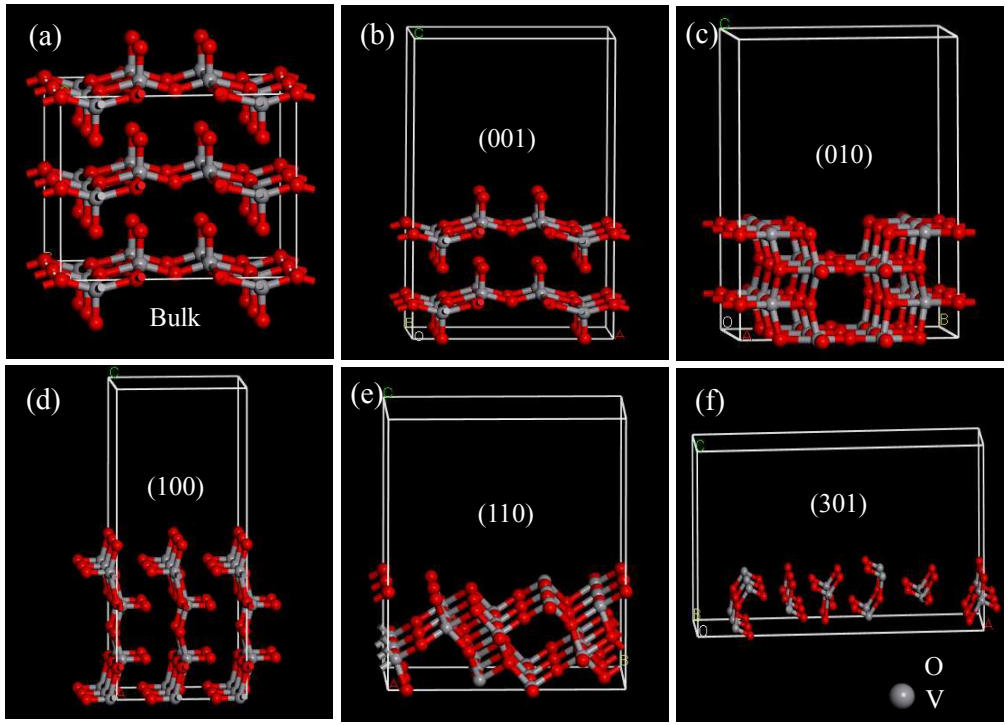

Fig. 11 Calculation modes of orthorhombic V_2O_5 by Material Studios software (a) super cell units; (b–f) atomic configuration of (001), (010), (100), (110) and (301) facets.

Fig. 12

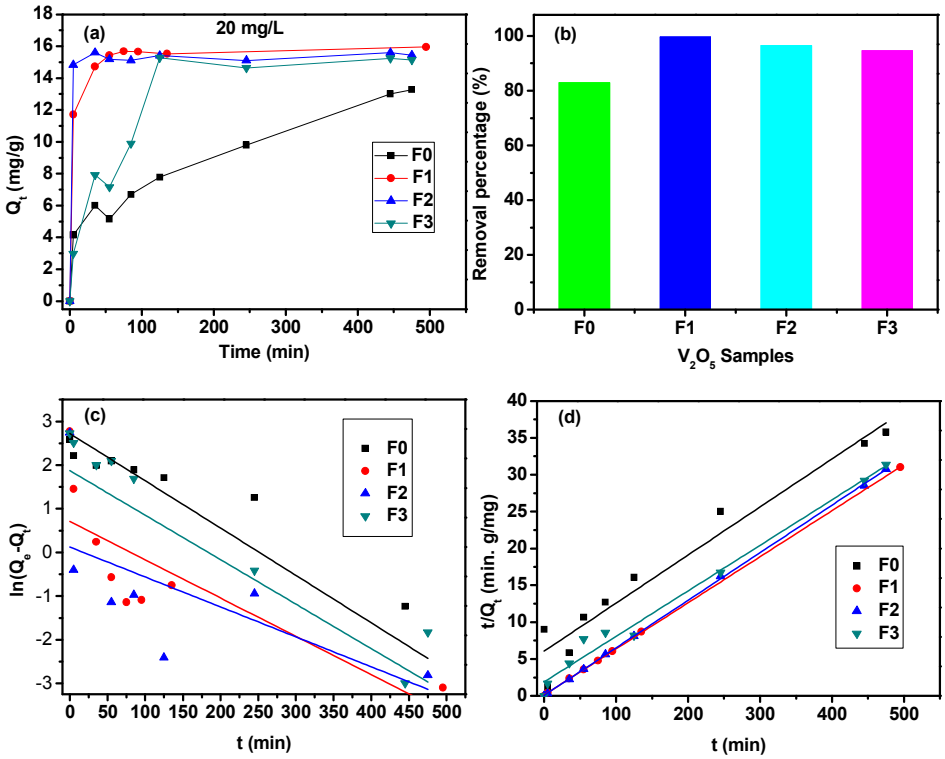

Fig. 12 The adsorption curves of MB (20 mg/L) over different V_2O_5 samples (the adsorbent dose was 1.25 g/L) (a) effect of contact time on adsorption; (b) remove rate over samples; (c) pseudo-first-order; (d) pseudo-second-order.

Fig. 13

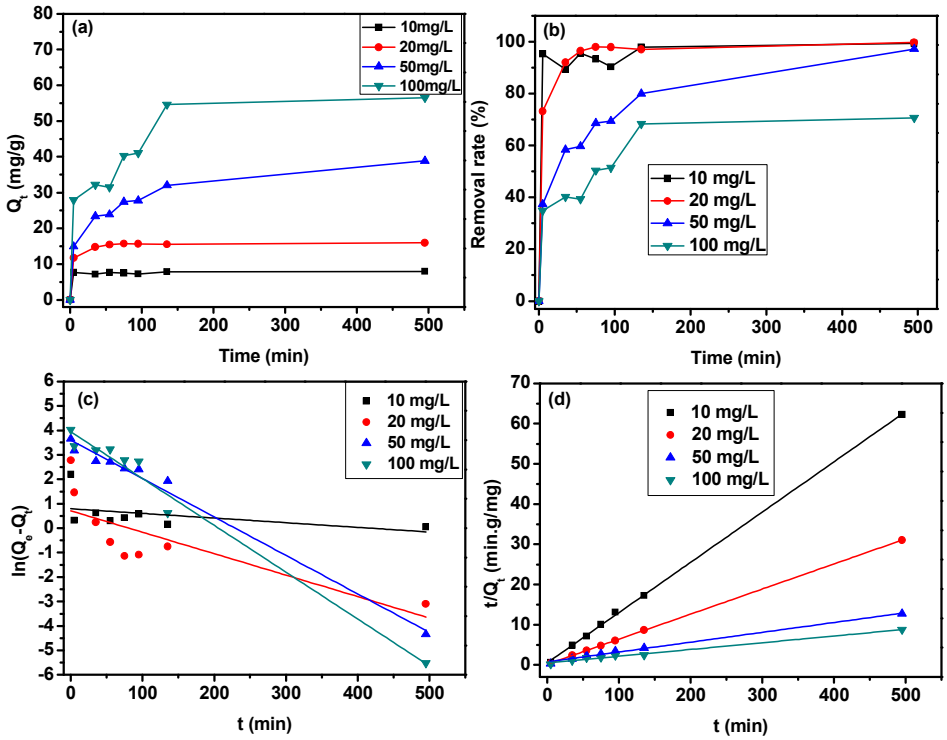

Fig. 13 Effect of initial MB concentration on the adsorptive performance at 298 K (a) effect of contact time on adsorption; (b) effect of contact time on remove rate; (c) pseudo-first-order; (d) pseudo-second-order.

Fig. 14

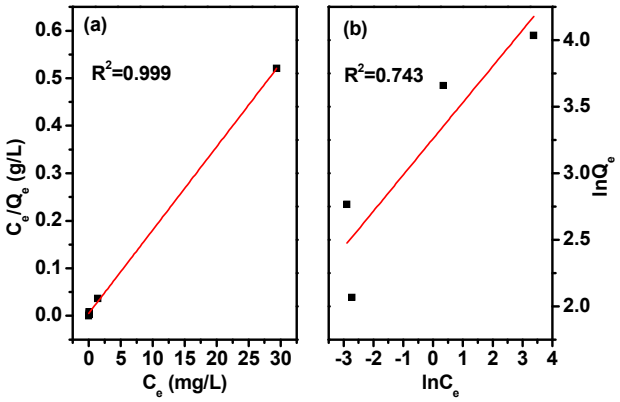

Fig. 14 The equilibrium isotherm for MB adsorbed by sample F1 (a) Langmuir model; (b) Freundlich model.